PHYSICAL REVIEW B **79**, 205409 (2009)

Facets of nanotube synthesis: High-resolution transmission electron microscopy study and density functional theory calculations

Gavi E. Begtrup, Will Gannett, and Jannik C. Meyer
Department of Physics, University of California–Berkeley, Berkeley, California 94720, USA
and Materials Sciences Division, Lawrence Berkeley National Laboratory, Berkeley, California 94720, USA

Thomas D. Yuzvinsky
Department of Physics, University of California–Berkeley, Berkeley, California 94720, USA;
Materials Sciences Division, Lawrence Berkeley National Laboratory, Berkeley, California 94720, USA;
and Center of Integrated Nanomechanical Systems, Berkeley, California 94720, USA

Elif Ertekin
Berkeley Nanosciences and Nanoengineering Institute, Berkeley, California 94720, USA

Jeffrey C. Grossman
Center of Integrated Nanomechanical Systems, Berkeley, California 94720, USA
and Berkeley Nanosciences and Nanoengineering Institute, Berkeley, California 94720, USA

Alex Zettl
Department of Physics, University of California–Berkeley, Berkeley, California 94720, USA;
Materials Sciences Division, Lawrence Berkeley National Laboratory, Berkeley, California 94720, USA;
and Center of Integrated Nanomechanical Systems, Berkeley, California 94720, USA
(Received 25 February 2009; published 14 May 2009)

We report the presence of catalytically active facets on iron nanocrystals during carbon nanotube synthesis. Using real-time *in situ* high-resolution transmission electron microscopy, we observe the facets' formation and interaction with carbon feedstock and are able to infer carbon diffusion across the catalyst surface facilitating nanotube formation. The observations are supported by density functional theory calculations.

DOI: 10.1103/PhysRevB.79.205409 PACS number(s): 81.07.De, 61.46.Df, 68.35.Fx

I. INTRODUCTION

Carbon nanotubes (CNTs) are appealing materials for electronic, phononic, optical, and mechanical systems applications. However, since small variations in nanotube geometry can strongly affect physical properties, many nanotube-based technologies necessitate precise control over nanotube defect structure, diameter, and chirality. Although it is well known that transition-metal catalysts enable different forms of nanotube growth, there is a surprising lack of knowledge of the catalytic growth process. Even fundamental questions such as the physical state of the catalyst, the mode of carbon diffusion along or through the catalyst and the means by which feedstock organic compounds are converted into atomic or molecular carbon during nanotube synthesis are unanswered.

II. EXPERIMENTAL METHOD

A powerful technique for the study of such growth employs *in situ* environmental transmission electron microscopy (TEM),[1–3] where CNT growth occurs within a sealed, secondary compartment placed within the microscope. In the experiments here described, we employ a large-diameter multiwalled carbon nanotube[4–6] as a nanoscale reaction chamber. In addition to increasing resolution, this configuration allows precise control of the reaction temperature, the geometry of the catalyst particle, and the source rate of feedstock material during CNT growth. Figure 1 shows the synthesis configuration in simplified schematic form. Carbon feedstock consisting of organic molecules, amorphous carbon, or graphitic carbon is located within the growth chamber in close proximity to the catalytic iron nanoparticle. The reaction temperature is controlled by Joule heating via an applied electrical current through the walls of the chamber. The entire system is mounted on a specially fabricated electron-transparent silicon nitride membrane and imaged with a high-resolution TEM (JEOL 2010, operated at 100 keV).

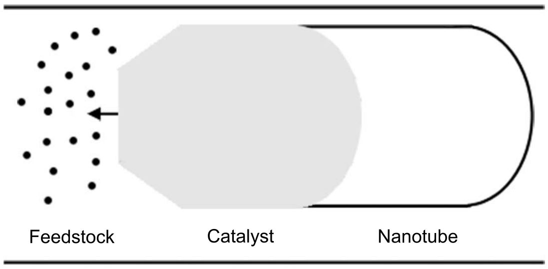

FIG. 1. Solid-state growth of a CNT: a faceted catalyst particle removes carbon from a feedstock. The carbon surface diffuses to the opposite end of the catalyst and precipitates as a nanotube. The arrow shows the direction of motion of the catalyst relative to the feedstock.

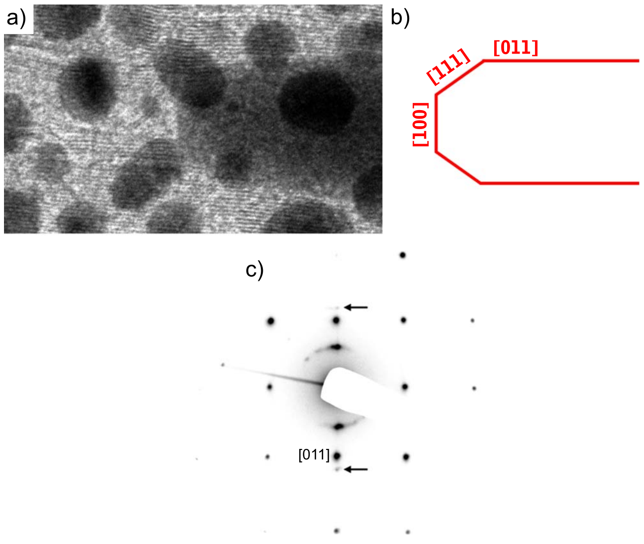

FIG. 2. (Color online) Orientation of the catalyst facets: (a) a typical leading edge of the iron catalyst in contact with the inner nanotube walls during the synthesis showing the flat front and angled facets. The dark round objects are gold position markers external to the nanotube. The angle between the front and angled facets is 55°, close to the expected 54.75° between (100) and (111) planes of α iron. (b) A drawing indicating the labeling of the facets in (a). (c) Nanobeam diffraction of a typical encapsulated iron particle indicating bcc crystal structure. The nanotube wall spacing is indicated by the arrows and is parallel to the labeled [011] iron diffraction peak.

In practice, we find it advantageous to immobilize solid-state carbon feedstock with respect to the reaction chamber and, using an electrical-current induced electromigration mechanism, move the catalytic particle with respect to the reaction chamber into the feedstock. In this way, encapsulated amorphous carbon or even the innermost walls of the nanotube reaction chamber itself can be consumed as source material for CNT growth. Catalyzed carbon diffuses along the catalyst in the direction of the current, consistent with electromigration of carbon in bulk iron.[7] As the carbon diffuses and the CNT grows from the trailing edge of the catalyst particle, the catalyst is displaced in the direction opposite the current, driving it into further carbon feedstock and continuing the growth. The direction of the applied current can be reversed at any time, thus reversing the direction of catalyst motion and CNT growth. Thus a newly grown nanotube can be deconstructed atom by atom.

Figure 2(a) shows a TEM image for a selected experiment. The horizontal striations running left to right across the upper and lower portions of the image represent concentric shells of the multiwall nanotube reaction chamber. The large dark object covering much of the right half of the image is the encapsulated iron catalyst particle. The smaller circular and oblong dark spots randomly distributed over the image represent gold nanoparticles intentionally deposited over the outside of the reaction chamber; these serve as absolute position markers and also as local thermometers for high-temperature measurements.[8]

The state of the catalyst particle is of primary interest both during hot CNT growth and in quiescent quench mode (with the drive current set to zero and the reaction chamber at room temperature). We employ nanobeam (~100 nm beam size) electron diffraction in the TEM to characterize the catalyst. Figure 2(c) shows diffraction data, which are consistent with solid iron in the α phase (the bcc crystal structure and the stable bulk allotrope at typical temperatures and pressures). The [100] axis of the iron crystal is aligned with the longitudinal axis of the reaction chamber. In addition, close examination of the catalyst in Fig. 2(a) shows that the left (leading) edge of the crystal is distinctly faceted. Figure 2(b) shows a tracing of the facet structure with different crystallographic faces identified. As we discuss below, this facet structure is a key element in the functionality of the catalyst particle during CNT growth.

By precisely controlling the applied electrical drive current, we observe the atomic structure of the catalyst throughout different stages of CNT growth. From real-time diffraction patterns and dark field imaging we find that the catalyst particle remains *solid and crystalline* throughout the CNT growth process. This is not to say, however, that the *shape* of the catalyst particle remains unchanged. Indeed, during CNT growth, the facet structure of both the leading and trailing edges of the catalyst evolve (via solid-state transformation) in response to varying availability of feedstock material. The catalytically active leading edge (the one receiving and disassembling sufficient carbon feedstock) is always found to be highly faceted, while the trailing edge (where the CNT is atomically assembled) has no observable facets. When we reverse the growth direction, the leading and trailing edges of the catalytic particle interchange and the facet structure switches concomitantly from one end of the catalyst to the other.

Figure 3 shows details of the facet geometry of the catalyst's leading edge during different stages of the CNT growth process. In Fig. 3(a), during initial stages of movement, large (111) facets and strong catalytic activity result in CNT growth (this occurs to the right and is not shown in these images). The (111) facets are present in response to the abundance of carbon feedstock, in the form of graphitic layers. As feedstock becomes less abundant, the (111) facets adjust accordingly, successively shrinking in size [Figs. 3(b)–3(d)]. When all carbon feedstock is exhausted [Fig. 3(e)], the (111) facets disappear altogether and CNT growth ceases.

Figure 4 shows the complementary geometry at the catalyst particle's trailing edge. As seen in Figs. 4(a) and 4(b), the iron nanoparticle moves against the current as carbon atoms electromigrate in the opposite direction. Carbon atoms diffuse to the cathode and cover the surface, inducing a change in its shape [Fig. 4(c)]. With the addition of more carbon [Fig. 4(d)] a double-walled nanotube endcap is extruded from the rounded iron cathode. Further carbon drives the growth and nanotube walls are extruded. The observations of this growth process are consistent with theoretical predictions of carbon surface saturation and end cap formation on the surface of a catalyst.[9] We note that during growth, unlike the leading edge, the trailing edge of the catalyst does not exhibit facets which may be attributed to surface roughening. Since the trailing edge is always carbon saturated (as opposed to graphene terminated as on the leading edge) and the relative differences in carbon saturated (100) and (111)

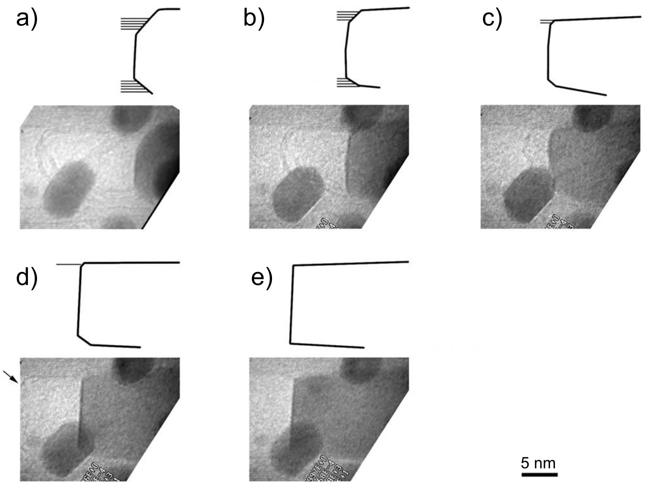

FIG. 3. Tracking facet structure: frames from video of the leading edge of the catalyst accompanied by outlines of the catalyst and incoming carbon source in the form of graphitic layers. Note that some layers are obscured by gold markers. Current is applied from left to right in the images. (a) The catalyst begins moving forward (left) with many feedstock layers interacting with the angled (111) facets. [(b)–(d)] The innermost layers of the source become absorbed as the catalysts progresses and the (111) facets decrease in size. (d) An arrow points to the last source layer. (e) The source is completely exhausted and the (111) facets disappear. Nanotube growth is no longer possible.

surface energies are small, one might expect the trailing edge to roughen at lower temperatures than the leading edge. At the elevated synthesis temperatures in our experiment, the trailing surface becomes roughened, as observed. These surface energies will be explained in the following model calculations section.

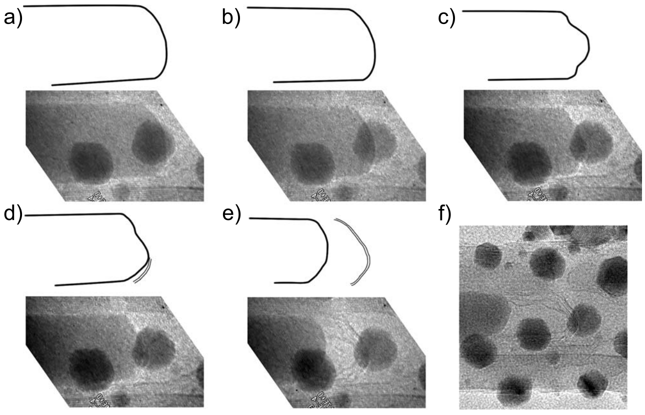

FIG. 4. Nanotube growth at the cathode of the catalyst. [(a)–(e)] Frames from video of the *in situ* nanotube growth at the trailing edge of the catalyst accompanied by outlines of the catalyst and parts of the extruded nanotube. Note that some layers are obscured by gold markers. Current is applied from left to right in the images. (a) The iron nanoparticle catalyst prior to application of current. (b) The catalyst begins to move right. (c) Carbon begins to cover the trailing edge (right, cathode), causing the shape to change. (d) CNT walls begin to lift off of the catalyst. (e) A multiwalled carbon nanotube (MWCNT) is grown off of the catalyst. (f) A high-resolution image of the nanotube after growth.

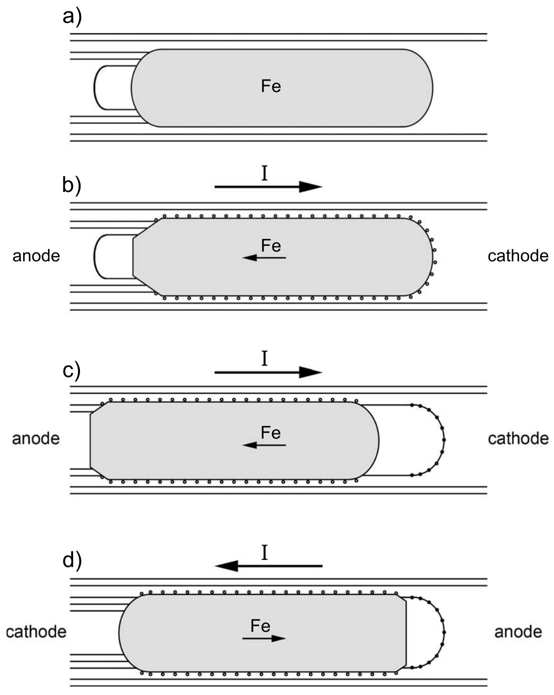

FIG. 5. Schematic of *in situ* nanotube synthesis: a metal encapsulated MWCNT with the outer nanotube walls as the synthesis chamber, the encapsulated metal (gray) as the catalyst, and the internal walls of the MWCNT or amorphous carbon as the source. (a) The system as synthesized. (b) As current is applied, carbon electromigrates along the surface in the direction of the current and facets form at the anode. The carbon supersaturates at the cathode. (c) Carbon moving in the direction of the current along the catalyst pushes the catalyst against the current, driving further catalysis of the carbon source and growth of a nanotube. Changes in the carbon feedstock cause the facets to evolve. (d) By reversing the applied current, the reaction is reversed. Facets form at the new anode and the newly grown nanotube is consumed.

Figure 5 schematically summarizes our observations of facet evolution and nanotube growth. Figure 5(a) shows the unfaceted iron catalyst in the as-prepared system. Application of current causes (111) facets to form at the leading (left) edge of the iron (anode) where catalysis of the carbon feedstock occurs [Fig. 5(b)]. Catalyzed carbon diffuses along the catalyst in the direction of the current and coats the opposite trailing end of the catalyst (the cathode). The iron catalyst is displaced in the direction opposite the current, driving it into further carbon feedstock and further loading it with carbon. Excess carbon is released via growth of a carbon nanotube at the trailing (right) edge of the catalyst [Fig. 5(c)]. While the carbon quantity is conserved, the newly synthesized nanotube may be of a different geometry than the carbon feedstock and thus may be both longer and of fewer walls, as portrayed here. Reversal of the applied current [Fig. 5(d)] causes facets to form on the opposite end of the catalyst (the new anode) as the iron consumes the newly formed nanotube and precipitates a multiwalled nanotube at the left end (new cathode).

Although in the present experiments the iron nanoparticle catalyst is constrained within a large-diameter multiwalled nanotube reaction chamber, our observations have relevance to more conventional chemical vapor deposition (CVD) growth using transition metal catalysts including iron. Under CVD growth conditions, applied chemical and thermal gradients might be expected to cause nanoparticle reshaping and facet formation resulting in nanotube growth similar to that described here. If, on the other hand, the catalyst particle is molten during CVD growth, the catalytic action and growth mechanism are expected to be markedly different.

We now turn to a theoretical analysis of our catalyst system to elucidate the metal-nanotube interactions.

III. MODEL CALCULATIONS

Due to their extremely high surface-to-volume ratios, catalyst nanoparticles are highly susceptible to environmental changes[10] which affect the relative stabilities of their different surfaces. During synthesis, we observe in the leading edge of the catalyst that the iron (111) facets grow (or shrink) to accommodate larger (or smaller) numbers of internal nanotube wall feedstock. In order to understand this change, we have performed *ab initio* calculations based on density functional theory (DFT) of the relative energies of different α-iron surfaces.

All density functional theory calculations reported in this work are conducted within the Perdew-Burke-Ernzerhof generalized gradient approximation (GGA-PBE) to the exchange-correlation potential[11] as implemented within the Vienna *ab initio* simulation package (VASP).[12,13] We conduct spin-polarized calculations and represent the atoms using the projector augmented wave (PAW) pseudopotentials[14,15] provided with VASP. All atoms are relaxed so that interatomic forces are less than 0.02 eV/Å. We use a plane-wave cutoff of 420 eV, which is sufficient for the convergence of binding energies in the iron slabs. For all calculations reported, we have ensured accurate sampling of the Brillouin zone via k-point convergence. The results reported here are converged to the number of significant figures shown.

For all surface calculations, we use at least six layers of iron and leave a large vacuum (~10 Å) between layers so that adjacent slabs do not interact from the periodic boundary conditions. For the surface calculations, we use the lattice constant for bcc iron as predicted by the GGA (2.84 Å, which is within 0.01 Å of the experimental value). Before adding carbon atoms, we relax the bare iron (100), (110), and (111) surfaces alone.

To compute binding energies of isolated carbon atoms, for the (100) surface, we use a (4×4) unit-cell reconstruction; for the (111) surface, a (3×3) unit-cell reconstruction; and the (110) surface, a (2×3) reconstruction. The binding energy is defined here as the difference in energy between (1) an isolated carbon atom and a fully relaxed iron surface and (2) the fully relaxed energy of the iron surface with the carbon atom adsorbed. We sample carbon adsorption energies at a variety of sites on each surface, as illustrated in Fig. 6. For each, the binding energy is determined by allowing iron atoms to relax as desired and carbon atoms to relax in the direction normal to the surface; values are reported in Table I. We also report binding energies of carbon atoms when the surface is *fully saturated* (meaning here that a carbon atom is placed at the most favorable location in each unit cell of the surface), for which our results are in excellent agreement with prior similar calculations (accounting for the nonzero energy of an isolated carbon atom).[16]

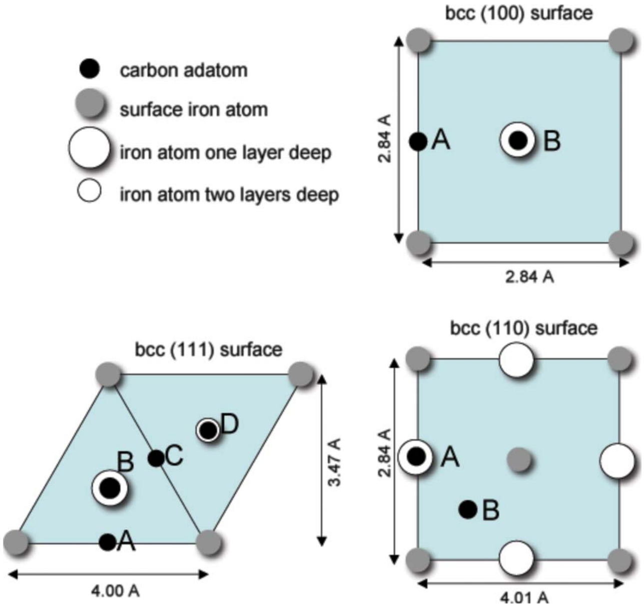

FIG. 6. (Color online) Top view of (1×1) unit cells for (100), (111), and (110) surfaces showing sites for adsorbed carbon atoms. The black circles represent carbon adatoms, the gray circles are surface iron atoms, and the white circles represent one and two layer deep iron atoms.

We now describe how to compute the surface excess energies of iron surfaces that are (1) saturated with carbon atoms as described above [Fig. 7(a)] or (2) have graphene layers penetrating perpendicular to the surface [Fig. 7(b)]. We define the surface excess energy here as the energy penalty associated with terminating an iron surface with nanotube walls with a specified orientation to each other. As such, it is the difference between the computed energy of the in-

TABLE I. Summary of binding energies (as defined in the text) of carbon atoms on iron surfaces. The sites sampled correspond to the locations indicated in Fig. 6.

Surface	Geometry	Site	Binding energy (eV)
bcc (100)	[4×4×3]	A (isolated)	7.22
bcc (100)	[4×4×3]	B (isolated)	9.34
bcc (100)	[1×1×3]	B (saturated)	6.85
bcc (111)	[3×3×3]	A (isolated)	7.60
bcc (111)	[3×3×3]	B (isolated)	1.59
bcc (111)	[3×3×3]	C (isolated)	7.41
bcc (111)	[3×3×3]	D (isolated)	7.60
bcc (111)	[1×1×3]	D (saturated)	6.29
bcc (110)	[2×3×3]	A (isolated)	7.97
bcc (110)	[2×3×3]	B (isolated)	6.96
bcc (110)	[1×1×3]	B (saturated)	6.56

(a) Wulff construction using C-saturated (111) surface

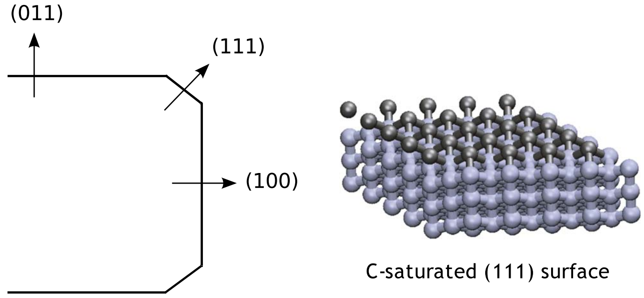

(b) Wulff construction using graphenated (111) surface

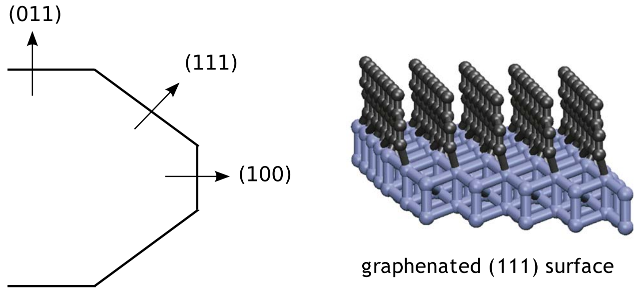

FIG. 7. (Color online) Wulff constructions showing equilibrium facet structures for α-iron catalysts with different surface terminations. For both structures, the (011) surface is terminated with an overlying parallel layer of graphene. (a) Wulff construction obtained using carbon saturated (100) and (111) surface energies. (b) Wulff construction obtained using carbon saturated (100) and graphene terminated (111) surface energies. The different facet structures correspond well with the changes observed in experiment as impingent graphene layers are consumed.

terfaced system and the energy of the same number of bulk bcc iron atoms (total energy of 8. 312 eV/atom) and carbon atoms in graphene (total energy 9. 267 eV/atom). By dividing by the total area of surface present, we obtain a surface excess energy density. Table II reports the surface excess energies that we have computed. We have also computed the surface energy of the (110) surface with a layer of graphene lying parallel to the surface to represent the geometrical constraints of the catalyst in our experiment. This surface is illustrated in Fig. 8 below.

The reported values indicate that as the length of the nanotube walls drop (that is, as nanotube walls are consumed during catalysis), the surface excess energy between the iron and the nanotubes increase. As the nanotube is consumed during catalyst motion, the surface energy of the (111) face should vary from the “graphenated” to the “saturated” value corresponding to the observed change in facet structure. As a final note, both the saturated surfaces and penetrating graphene layers can be constructed in a variety of ways, which may affect quantitatively the value of the surface energy obtained. For the various surfaces with penetrating or parallel graphene layers, we have chosen orientations which strain the graphene unit cells so that it is commensurate with the iron surface; we selected orientations that minimize strain as much as possible while maintaining a reasonable system size for computation. This results as well in different surface densities of carbon atoms, which are reported in Table II. Although our calculations compare surface energies for very particular geometries, the result that the catalyst’s surface energy increases as the length of the penetrating graphene sheet drops is generally applicable.

TABLE II. Summary of surface excess energy densities (as defined in the text) between bcc iron and graphene for various structures of the interface. The excess surface energies are referenced to bulk bcc iron atoms and carbon atoms in graphene. The resulting quantities demonstrate that the surface energy varies with the structure of the interface: the surface energy increases as the nanotube walls are consumed. This increase in surface energy is consistent with the observed change to the structure of the catalyst as it moves through the system and catalyzes the nanotube walls.

Surface	Description	Surface energy (eV/A^2)	C density (A^2 per C)
bcc (100)	Saturated	0.303	8.032
bcc (100)	Penetrating graphene	0.218	10.709
bcc (111)	Saturated	0.292	13.871
bcc (111)	Penetrating graphene	0.222	8.670
bcc (110)	Saturated	0.284	11.330
bcc (110)	Penetrating graphene	0.237	5.665
bcc (110)	Parallel graphene	0.190	2.550

Figure 7 shows the Wulff construction of the iron catalyst obtained using surface energies computed from the DFT calculations for two different conditions. In Fig. 7(a), we model the nanoparticle after the feedstock has been exhausted; the iron (111) and (100) facets are both saturated with carbon atoms, resulting in a Wulff structure with small (111) facets. In contrast, in Fig. 7(b), to model the system during catalysis, we apply the surface energy of the iron (111) surface terminated by perpendicular graphene sheets [but keep the (100) facet saturated with carbon atoms]. Because the (111) surface has lower energy when graphene terminated than when carbon saturated, the Wulff construction shows enhanced (111) facets when graphene terminated, corresponding well to the behavior we observe in the experiments. Although these calculations consider only several

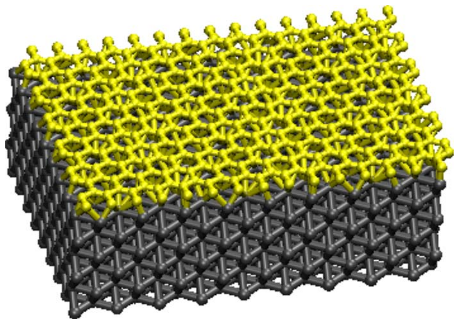

FIG. 8. (Color online) Illustration of the (110) iron surface in contact with a parallel graphene layer. This interface geometry between graphene and iron models the nanotube walls encapsulating the catalyst particle on the periphery of the system.

representative cases for carbon/Fe-surface termination structures, they nonetheless indicate that relative changes in surface energies for different surface terminations can explain the catalyst shape changes observed.

IV. RELATIVE ENERGIES AND DIFFUSION CONSIDERATIONS

We note that the feedstock graphitic walls are never observed to intersect the (100) surface even though its graphene-terminated surface energy is lower than that of the graphene-terminated (111) surface. In order to understand this, we first note that the nanotube walls are constrained to the outer edge of the chamber. We then compare the relative energies of two distinct particle shapes: (1) a flat-faced catalyst with no (111) facets, with a portion of the (100) surface graphene terminated and the remainder carbon saturated, and (2) a catalyst with (100) and (111) facets, with only the (111) surface graphene terminated. Comparing the relative energies of these systems at overall equal portions of graphene termination, we find the total energy of the latter system (the structure that we observe in our experiments) to be lower for graphene-termination coverage below a critical threshold. Below the threshold, the equilibrium structure is predominately determined by a minimization of total surface area and (111) facets are stable; however, beyond the threshold, the lower surface energy of the (100) facet dominates, causing the (111) facets to disappear. Consistent with this prediction, our experiments take place in the former regime.

Once the iron has catalyzed the dissociation of the carbon source, newly deposited carbon atoms on the leading catalyst surface must diffuse along the (110) plane to the trailing edge of the nanoparticle for CNT synthesis to proceed. We now consider two different models of the migration of carbon in the iron catalyst: bulk diffusion and surface diffusion.

For bulk diffusion to occur, carbon must dissolve into the iron catalyst. However, α iron has very low carbon solubility, with a maximum at 0.028 wt %, 2 orders of magnitude lower than that of γ (fcc) iron. As carbon solubility has been expected to predict catalyst suitability,[17] confirmation of growth in bcc iron is surprising and perhaps unprecedented. Additionally, theoretical studies have found that the energy required for a carbon atom to penetrate into the center of a nanoparticle is prohibitively high.[18] The iron-carbon phase diagram shows that the solubility of carbon in bcc iron increases as the temperature rises in the relevant temperature range. Were bulk diffusion to dominate the carbon migration, the iron would be nearly saturated during synthesis. Rapid cooling of the system and the resulting decrease in carbon solubility would thus cause either precipitation of carbon out of the iron or the formation of a carbide phase. We quench the hot nanoparticle by zeroing the current, but we do not observe either of these phenomena, suggesting that surface or subsurface diffusion of carbon on the iron dominates over bulk diffusion.

V. CONCLUSIONS

By directly observing and controlling nanotube synthesis *in situ*, we are able to observe catalytic action in real time. Subsequent modeling of the carbon/catalyst system using density functional theory reveals surface energy differences between crystal faces that depend on the presence of carbon. These energy differences can explain the changes in catalyst particle shape observed during synthesis. Furthermore, these observations suggest that the carbon travels from the catalysis site to the growing nanotube by diffusion along the {100} surfaces of the iron.

ACKNOWLEDGMENTS

This work was supported by the Director, Office of Energy Research, Office of Basic Energy Sciences, Materials Sciences and Engineering Division, of the (U.S.) Department of Energy under Contract No. DE-AC02-05CH11231. A.Z. acknowledges support from the Miller Institute for Basic Research in Science. W.G. acknowledges support from the NSF Integrative Graduate Education and Research Traineeship (IGERT) Program. J.C.G. and E.E. acknowledge funding by the Focus Center Research Program on Materials, Structures, and Devices (FCRP/MSD). Computations were performed at the National Energy Research Scientific Computing Center.

---

[1] R. Sharma and Z. Iqbal, Appl. Phys. Lett. **84**, 990 (2004).

[2] M. Lin, J. P. YingTan, C. Boothroyd, K. P. Loh, E. S. Tok, and Y.-L. Foo, Nano Lett. **6**, 449 (2006).

[3] S. Helveg, C. Lopez-Cartes, J. Sehested, P. L. Hansen, B. S. Clausen, J. R. Rostrup-Nielsen, F. Abild-Pedersen, and J. K. Norskov, Nature (London) **427**, 426 (2004).

[4] K. Jensen, W. Mickelson, W. Han, and A. Zettl, Appl. Phys. Lett. **86**, 173107 (2005).

[5] K. Svensson, H. Olin, and E. Olsson, Phys. Rev. Lett. **93**, 145901 (2004).

[6] J. A. Rodriguez-Manzo, M. Terrones, H. Terrones, H. W. Kroto, L. Sun, and F. Banhart, Nat. Nanotechnol. **2**, 307 (2007).

[7] H. Nakajima and K.-i. Hirano, J. Appl. Phys. **48**, 1793 (1977).

[8] G. E. Begtrup, K. G. Ray, B. M. Kessler, T. D. Yuzvinsky, H. Garcia, and A. Zettl, Phys. Rev. Lett. **99**, 155901 (2007).

[9] J. Y. Raty, F. Gygi, and G. Galli, Phys. Rev. Lett. **95**, 096103 (2005).

[10] P. L. Hansen, J. B. Wagner, S. Helveg, J. R. Rostrup-Nielsen, B. S. Clausen, and H. Topsoe, Science **295**, 2053 (2002).

[11] J. P. Perdew, K. Burke, and M. Ernzerhof, Phys. Rev. Lett. **77**, 3865 (1996).

[12] G. Kresse and J. Hafner, Phys. Rev. B **47**, 558 (1993).

[13] G. Kresse and J. Furthmuller, Phys. Rev. B **54**, 11169 (1996).

[14] P. E. Blochl, Phys. Rev. B **50**, 17953 (1994).

[15] G. Kresse and D. Joubert, Phys. Rev. B **59**, 1758 (1999).

[16] S. Hong, Curr. Appl. Phys. **3**, 457 (2003).

[17] C. P. Deck and K. Vecchio, Carbon **44**, 267 (2006).

[18] S. Hofmann, G. Csanyi, A. C. Ferrari, M. C. Payne, and J. Robertson, Phys. Rev. Lett. **95**, 036101 (2005).